SDR-Based Dual Polarized L-Band Microwave Radiometer Operating From Small UAS Platforms

Md Mehedi Farhad ⬤, *Graduate Student Member, IEEE*, Ahmed Manavi Alam ⬤, *Graduate Student Member, IEEE*, Sabyasachi Biswas ⬤, *Graduate Student Member, IEEE*, Mohammad Abdus Shahid Rafi ⬤, *Graduate Student Member, IEEE*, Ali C. Gurbuz ⬤, *Senior Member, IEEE*, and Mehmet Kurum ⬤, *Senior Member, IEEE*

Abstract—**Passive microwave remote sensing is a vital tool for acquiring valuable information regarding the Earth's surface, with significant applications in agriculture, water management, forestry, and various environmental disciplines. Precision agricultural (PA) practices necessitate the availability of field-scale, high-resolution remote sensing data products. This study focuses on the design and development of a cost-effective, portable L-band microwave radiometer capable of operating from an unmanned aircraft system platform to measure high-resolution surface brightness temperature (T_B). This radiometer consists of a dual-polarized (Horizontal polarized, H-pol and Vertical polarized, V-pol) antenna and a software-defined radio-based receiver system with a 30 MHz sampling rate. The post-processing methodology encompasses the conversion of raw in-phase and quadratic (I&Q) surface emissions to radiation T_B through internal and external calibrations. Radiometric measurements were conducted over an experimental site covering both bare soil within an agricultural field and a large water body. The results yielded a high-resolution T_B map that effectively delineated the boundaries between land and water, and identified land surface features. The radiometric temperature measurements of the sky and blackbody demonstrated a standard deviation of 0.95 K for H-pol and 0.57 K for V-pol in the case of the sky and 0.39 K for both H-pol and V-pol in the case of the blackbody observations. The utilization of I&Q samples acquired via the radiometer digital back-end facilitates the generation of different time–frequency (TF) analyses through short-time Fourier transform and power spectral density (PSD). The transformation of radiometer samples into TF representations aids in the identification and mitigation of radio frequency interference originating from the instrument itself and external sources.**

Index Terms—**Brightness temperature, L-band, microwave, precision agriculture (PA), radiometer, soil moisture (SM), unmanned aircraft system (UAS).**

I. INTRODUCTION

PASSIVE microwave radiometers capture the natural electromagnetic radiation emitted by the environmental features. They are highly sensitive to very small changes in the thermally emitted noise. The radiometric measurement of the Earth's surface can be used to estimate the surface soil moisture (SM), which is a critical parameter for precision agriculture (PA) applications [1]. The portion of microwave radiation that soil emits is heavily influenced by the moisture content of the soil. This is due to the fact that water molecules absorb and scatter microwave radiation in the L-band, hence the amount of thermal microwave radiation produced in the soil decreases as water content increases. By measuring the microwave radiation emitted from the soil, microwave radiometers can estimate the moisture content of the soil [2], [3], [4]. Field-scale high-resolution SM information is crucial for farmers to efficiently schedule irrigation and conserve the already scarce usable water. The L-band radiometer has been deployed from multiple platforms to retrieve high-resolution surface SM for PA applications in [5] and [6]. While optical and thermal sensors have traditionally been employed for precise SM retrieval, comparative analysis in [7] indicates that relying solely on the L-band passive microwave technique yields superior accuracy for SM estimation compared to thermal-optical methods. The passive L-band microwave radiometers operate in the protected band (1400–1427 MHz) with 27 MHz bandwidth, and a center frequency of 1413.5 MHz [8].

European Space Agency (ESA) launched an L-band microwave radiometer satellite called Soil Moisture and Ocean Salinity (SMOS) in November 2009 for the remote sensing of surface SM and ocean salinity globally [9]. Later, the National Aeronautics and Space Administration (NASA) launched another L-band microwave radiometer named Soil Moisture Active Passive (SMAP) satellite in January 2015 [10]. The SMOS and SMAP radiometers have a ground resolution on the order of 30–40 km with a revisit time of 1 to 3 days [11], [12]. The coarse spatial resolution of spaceborne radiometers limits its use in PA applications that need the SM information at subfield scale resolution [13].

To obtain high ground resolution for radiometric measurement, various airborne radiometers have been developed, showing the potential to estimate geophysical parameters of the Earth's surface [14], [15], [16], [17]. A fully polarimetric

airborne radiometer has been developed in support of ESA for the measurement of sea surface signatures and salinity, SM, and the homogeneity of the Antarctic SMOS calibration site [18]. The Technical University of Denmark built the Cooperative Airborne Radiometer for Ocean and Land Studies (CAROLS) to measure ocean salinity and SM. The radiometer measures the microwave radiation emitted from the Earth's surface at a frequency of 1.4 GHz using a conical scanning antenna [19]. For measuring SM and ocean salinity, the Helsinki University of Technology developed an L-band airborne synthetic aperture radar (AIRSAR) radiometer. The radiometer used synthetic aperture radiometer technology to provide a high spatial resolution [20]. The L-band radiometry's performance for SM retrievals using data obtained from ground-based and airborne observations has been accessed. The ground-based observations were conducted at the University of Arizona's Remote Sensing Center of Excellence, while the airborne observations took place over the Texas High Plains, utilizing the NASA/JPL AIRSARand the University of Arizona's L-band radiometer. Results from the study demonstrated the viability of L-band radiometry for accurate SM retrievals. Furthermore, the precision of SM retrievals was notably enhanced when employing observations from multiple angles [21]. Although airborne L-band radiometers have shown potential for estimating high-resolution geophysical parameters of the Earth's surface, such as ocean salinity and surface SM, their usability for PA is restricted by overall expense and operation procedures. Similarly, while ground-based radiometers can produce high-resolution SM and vegetation data products, their usefulness for PA applications is limited due to their poor mobility and, coverage area [22], [23], [24], [25].

L-band microwave radiometer onboard a custom-grade unmanned aircraft system (UAS) offers more flexible operation compared with large airborne systems. A dual-polarized lightweight and compact L-band radiometer was developed by the authors in [8] and [26] for both UAS and ground-based applications. Their results unequivocally demonstrate that the radiometer can effectively and accurately measure both SM and snow water content. Furthermore, its lightweight design and portability render it highly adaptable for various field applications, broadening its potential utility in different contexts. Several lightweight, compact, and cost-effective radiometers for SM retrieval have been described in [27]. A ground base portable L-band microwave radiometer intended for the application of PA has been developed in [28]. The radiometer was tested on a variety of soil types with different moisture contents, vegetation covers, and solar radiation levels. The radiometer was also able to measure soil permittivity under a variety of environmental conditions.

A software-defined radio (SDR)-based L-band microwave has been developed for UAS-based application in [29] and [30]. SDR offers great control over the data acquisition rate, bandwidth, and radiometric output signal power. An SDR-based radiometer has also been developed in [31] that shows similar performance as the traditional radiometer [32], [33], [34]. Another UAS-based microwave radiometer was developed by Wan et al. [35] for high-resolution imaging of radiation brightness temperature (T_B).
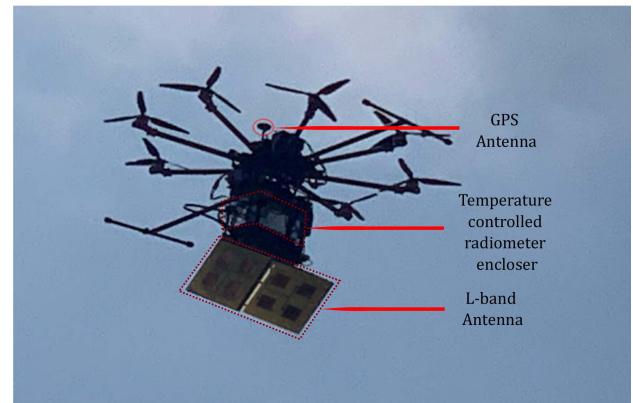

Fig. 1. L-band microwave radiometer flying on a custom-made octa-copter UAS platform. The dual-polarized antenna looking toward the ground at an angle of 45°. Close-up pictures and further details for the temperature controlled radiometer enclosure and antenna are provided in Figs. 3 and 4, respectively.

The radiometer was tested in an experimental demonstration area to image the T_B of different objects, including a water body, forest, and grassland. The results showed that the radiometer was able to estimate the T_B of the different objects with good contrast, and the boundaries of the objects were well-defined.

The primary objective of this study is to design and construct a portable L-band microwave radiometer to operate from a UAS platform using an SDR-based approach. Fig. 1 depicts the developed dual-polarized (horizontal polarized, H-pol and vertical polarized, V-pol) L-band microwave radiometer affixed underneath a custom-made octa-copter UAS platform. Radio frequency interference (RFI) presents a significant limiting factor for radiometric remote sensing measurements. Such interference may originate from both internal and external sources. Internally generated RFI arises from the radiometer instrument itself, while externally generated RFI can emanate from various active transmitter systems, such as active radar and communication systems [36]. A key innovation of this radiometer is its ability to access raw in-phase and quadratic (I&Q) samples, thereby enabling the evaluation of both conventional and data-driven RFI detection algorithms, as well as onboard real-time RFI mitigation [37], [38], [39], [40]. While detecting and mitigating RFI, the radiometer will simultaneously acquire new measurements for PA applications. In future studies, this radiometer will be a crucial part of a unique testbed for active communication and passive remote sensing coexistence research. This testbed will help to understand the effect of anthropogenic signals in the L-band radiometer with both in-band and out-of-band transmissions. The experiments will be conducted inside an anechoic chamber and a joint data-driven RFI detection, mitigation and calibration framework will be developed for this L-band radiometer [41], [42], [43]. The distinct contribution of this study can be summarized as follows.

1) This study proposes a near-real-time operation of a dual-polarized radiometer capable of operating from a UAS platform.
2) The radiometer's SDR-based digital back end allows us to have full control over the bandwidth, gain, sampling rate, and integration time.
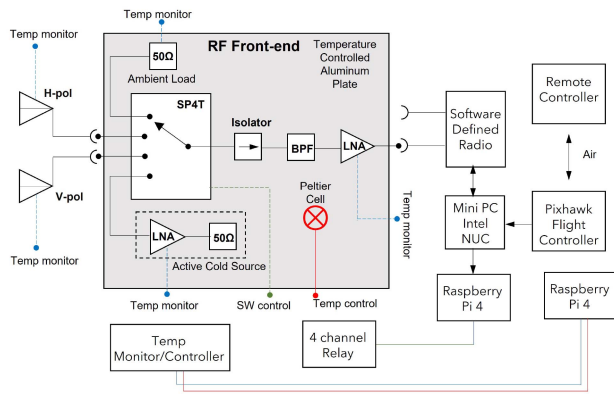
Fig. 2.   Design schematic of a dual-polarized L-band microwave radiometer.

3) We controlled the radiometer's internal temperature to reduce temperature-driven noise fluctuations.
4) The radiometer has been calibrated for five different internal temperatures to calculate the calibration coefficient for each internal temperature setting.
5) Onboard data processing helps to free up limited storage capacity and remove a large portion of instrument-generated RFI while receiving new data on the UAS platform.

The rest of this article is organized as follows. Section II describes the design schematic, radiometer packaging, dual-polarized antenna design and fabrication, data processing, and radiometric calibration to estimate the T_B. Section III presents and evaluates the antenna characteristics, data cleaning to remove RFI, each step of the calibration, and finally the T_B estimation. The implication of the findings discussed in Section IV. Finally, Section V summarizes this study and discusses the potential future work.

II. DESIGN AND IMPLEMENTATION

This section describes the details of the radiometer from design schematic to compact packaging, radiometric calibration, which includes internal and external calibration, system performance, processing of the radiometer raw data, and finally, the building of the octa-copter UAS platform.

A. Design Schematic of Radiometer Payload

The radiometer hardware design has three stages. The radio frequency (RF) front-end design, the digital back-end processing, and finally, the dual-polarized array antenna design and characterization. Radiometer front-end and back-end design are elaborated in the following sections. Fig. 2 depicts the design schematic of the dual-polarized L-band microwave radiometer.

1) RF Front-End Design: The radiometer's front-end consists of all the RF components. In Fig. 2, the RF front-end starts with a single pole four-through (SP4T) RF relay. The pole of the relay can be controlled to switch with a specific time delay for each through from external triggering. The SP4T RF relay used here works optimally within a 1 to 3 GHz band with an insertion loss of 0.5 dB. The H-pol and V-pol antennas are

connected to the 2-port of the RF relay. The other two ports of the RF relay are connected to 50-Ω matched loads, serving as an ambient reference load or hot source (HS), and a reverse low-noise amplifier (LNA) terminated with a 50-Ω matched load, serving as an active cold source (ACS). The four ports of the SP4T RF relay are connected to the dual-polarized antenna and reference loads followed by a 20 dB RF isolator. The RF isolator ensures unidirectional signal flow and prevents back-propagation of signals. The RF isolator exhibits an insertion loss of 2.17 dB and an optimum frequency range of 1 GHz to 2 GHz. The custom bandpass (BP) RF filter was connected after the isolator, followed by an LNA. The BP filter operates from 1400 to 1427 MHz and has an insertion loss of 2.6 dB at the center frequency of 1413.5 MHz. The LNA has a minimum frequency of 1.2 GHz and a maximum frequency of 1.6 GHz. The noise figure (NF) of this RF amplifier is significantly low, at 0.8 dB, with a typical gain of 40 dB. The LNA is rated at 15 V dc maximum and 120 mA. There is an additional loss due to all connectors and SMA sections of 0.5 dB. The entire RF front-end was placed on a temperature-controlled aluminum plate, which maintained the RF components at a predefined temperature throughout the operating time. The temperature control of the RF components helps to reduce the random variation of the noise.

2) Digital Back-End: The digital back-end of the radiometer consists of an SDR, Intel's Next Unit of Computing (NUC) mini PC, two Raspberry Pis, and a temperature controller unit. The SDR we used here is a National Instrument Universal Software Radio Peripheral B210 series. The SDR is directly connected with the RF front-end LNA. The radiometer operates through the Intel NUC mini PC. The NUC receives and stores the raw radiometric measurement data. One Raspberry Pi is responsible for triggering the SP4T RF relay for 250 ms per port. The RF front-end compensates for temperature drifts during each measurement cycle by performing calibration with its internal HS and ACS. During each cycle, the radiometer records raw data from each port of the RF switch for 250 ms, with a 250 ms integration time and 27 MHz full bandwidth within the protected L-band. The sampling rate of the radiometer data was 30 MHz. A second Raspberry Pi is responsible for recording the physical temperature of each RF component, including the H-pol and V-pol antennas and the RF coaxial transmission lines. A solid-state temperature controller known as a Peltier cell is used in conjunction with a digital control unit to control the temperature of the RF front-end.

3) Radiometer Packaging: All the components are packaged in a multilayered box. The RF components inside the box are placed on an aluminum plate, which is temperature-controlled using a Peltier cells temperature controller unit. As shown in Fig. 3, the first layer (bottom layer) holds all the RF components. The second layer (middle layer) consists of the SDR, power conversion units, Raspberry Pis, and electromechanical (EM) relays. The third layer (top layer) holds the temperature controller and power controller for the Peltier cell. Each component of the radiometer was subjected to individual measurements in order to observe its response and compare it against specification sheets, utilizing a network analyzer. Subsequent to the assembly of the radiometer, a comprehensive end-to-end
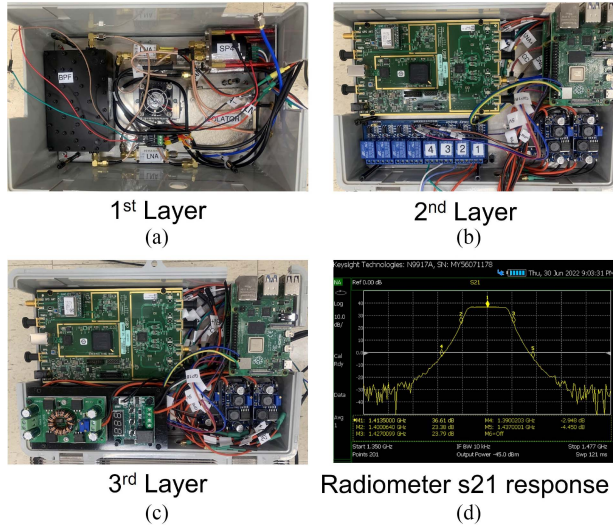
Fig. 3. Radiometer assembly is packaged within a multilayer compact structure and covered with aluminum tape. first layer (a) encompasses all the RF components integral to the radiometer. second layer (b) accommodates the SDR, EM relays, and Raspberry Pi units. Third layer (c) houses the temperature control unit along with six voltage converters. (d) Comprehensive radiometric response, as measured utilizing a network analyzer.

TABLE I
AIR-GAP PATCH ANTENNA DESIGN PARAMETERS

Parameter	Dimension (mm)	Parameter	Dimension (mm)
Wp	304.00	b	5.00
Lp	320.00	c	25.00
W	65.00	d	15.70
L	74.50	e	49.30
Wf	104.30	f	27.65
Lf	97.00	g	20.00
a	2.00	h	10.00

radiometric response analysis was conducted employing the network analyzer and shown in Fig. 3(d). More information about the radiometer power consumption and gross weight are detailed in Sections IV-B and IV-C.

4) Receiving Antenna: An air gap patch array antenna has been designed and simulated in the electromagnetic simulation environment. The near-square patch antenna was constructed on an Flame Retardant 4 (FR4) substrate with a dielectric constant of 4.3, tand δ of 0.025, and thermal conductivity of 0.3 (W/K/m). The thickness of the substrate was kept at 1.47 mm for both the front patch and the ground plane. The front plane and the ground plane were both designed with copper with a thickness of 0.035 mm. An air gap of 8 mm was introduced between the front patch and the ground plane to reduce the sidelobe and backlobe of the antenna. The design parameters and dimensions are given in Table I for the corresponding Fig. 4. The antenna feed port was designed with a coaxial feed SMA port. The antennas were fabricated using chemical etching. The antennas were tested with a network analyzer in the Mississippi State University (MSU)'s anechoic chamber. Both H-pol and V-pol antennas were attached to a frame for mounting on the UAS. Results related to the antenna characterization are detailed in Section III-A.
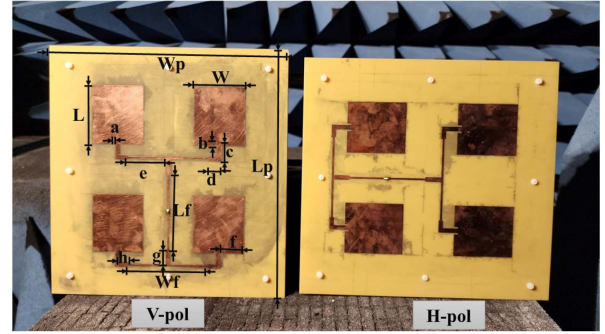

Fig. 4. V-pol and H-pol air-gap patch antennas were subjected to testing within an anechoic chamber. Both antennas share identical design parameters for their radiating or receiving patches. The ground plane for both antennas comprises an FR4 substrate material with a 1.47 mm thickness, having a 0.035 mm thick copper layer on one side.

B. Data Processing Steps

During data acquisition, the radiometer captures the surface emission as raw I&Q samples from the target source, storing the data in a short complex 16-bit (sc16) format. Transient responses were generated during RF port switching, which was subsequently eliminated from the data. The imperfect rise and fall time along with its transient response of the physical BP filter introduced an offset that was also corrected by applying a digital Butterworth filter with a 10 MHz cutoff frequency. Internal instruments of the radiometer, including the SDR, dc voltage regulators, and temperature controllers generate RFI that creates an unwanted bias in the radiometric measurement. This RFI was not necessarily visible in the time domain representation. This necessitates the implementation of time–frequency (TF) domain representation of the raw I&Q samples. The RFI was effectively addressed through the implementation of a percentile filtering technique. Specifically, an empirical approach was employed where a 99.7 percentile filtering threshold was selected. This selection was based on careful analysis and consideration, aiming to eliminate the RFI signals originating from the radiometer's internal components. By adopting the 99.7 percentile filtering technique, the presence of instrument-generated RFI was successfully mitigated in the frequency domain, resulting in enhanced data quality and accurate radiometric measurements. Subsequently, the frequency domain signals underwent a squaring process to transform them into raw power, achieved by squaring each individual sample. The results related to the data processing steps are further detailed in the Section III-B.

C. Calibration

This section describes the internal and external temperature calibration of the radiometer.

1) ACS Noise Temperature Characterization and Internal Calibration: The radiometer calibration is a critical step in converting the raw antenna count I&Q samples into T_B. The present radiometer uses two-point periodic internal calibration using an HS and an ACS noise source during each measurement cycle. The ambient noise source T_B is a direct measurement of
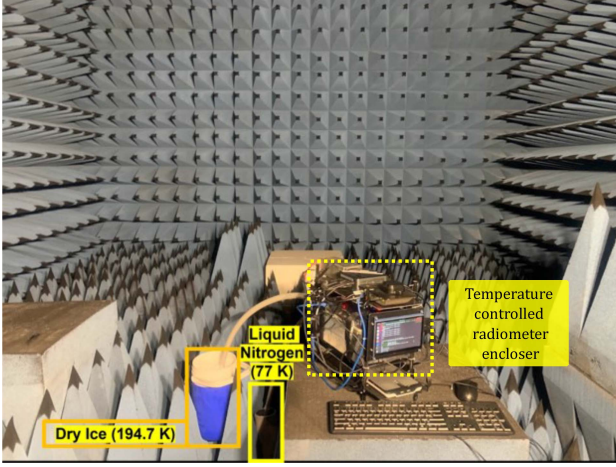
Fig. 5. Radiometer underwent internal temperature calibration using three sources: LN, DI, and the ambient source (HS). The experiment was conducted inside an anechoic chamber, where the physical temperature of the chamber was gradually increased from 299.15 to 307.15 K with an interval of 2 K over a period of $\sim$ 12 h.
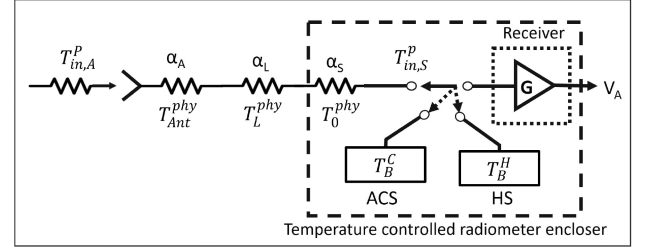

Fig. 6. Simplified block diagram to estimate the T_B of ACS through radiometer temperature calibration using LN, DI, and HS. Here, $T_{in,A}^P$ is the physical temperature of the LN and DI at the H-pol port and V-pol port, respectively. The symbol T_L^{phy} and α_L are the physical temperature and loss of the long transmission line respectively. The symbol T_0^{phy} and α_S are the physical temperature and loss of the short transmission line respectively. The symbol $T_{in,S}^P$ is the effective temperature of the input sources at the SP4T RF switch. The symbol V_A is the output voltage for the corresponding input sources (LN and DI). The symbol T_B^H and T_B^C are the physical temperatures of the HS and ACS ports. The symbol P corresponds to the polarization of the input port while connected to the receiving antenna. The symbol α_A and T_{Ant}^{phy} was used to estimate the antenna loss coefficient through external calibration.

the physical temperature of a 50-Ω load. However, the T_B of the ACS needs to be determined at different physical temperatures. Fig. 5 shows the calibration setup inside the anechoic chamber to determine the noise temperature of the "unknown" ACS using "known" sources, such as liquid Nitrogen (LN), dry ice (DI), and 50-Ω loads. The LN and DI have a boiling point temperature of 77 and 194.7 K, respectively, at atmospheric pressure; these sources are connected to the H-pol and V-pol ports of the radiometer. The internal physical temperature of the radiometer (T_0^{phy}) is kept constant during the operation of the radiometer.

The effective noise temperature ($T_{in,A}^P$) of each source (for instance, LN) passes through the transmission line, the switch, and several connectors; consequently, it emerges as $T_{in,S}^P$ at the receiver reference input. The output voltage from the receiver and the input temperature to the receiver are related by a linear equation as described in (1) and 2

$$G = \frac{V_A - V_H}{T_{in,S}^P - T_B^H} = \frac{V_C - V_H}{T_B^C - T_B^H} \quad (1)$$

$$N = \frac{V_A - V_H}{V_C - V_H} \quad (2)$$

where G is the overall system gain, and V_A is the output voltage for the corresponding input temperature from LN or DI. V_H and V_C are the output voltage readings due to the corresponding HS and ACS internal noise sources, respectively. T_B^C and T_B^H are the noise temperatures of ACS and HS, respectively. Finally, N is the normalized voltage value.

The effective noise temperatures of each of the sources (i.e., LN and DI) are calculated at the reference point in Fig. 6 using (3) and (4)

$$T_{in,S}^P = (1 - N) T_B^H + N T_B^C \quad (3)$$

$$T_{in,S}^P = T_{in,A}^P \alpha_L \alpha_S + T_L^{phy} (1 - \alpha_L) \alpha_S$$
$$+ T_0^{phy} (1 - \alpha_S) \quad (4)$$

where $T_{in,S}^P$ is the effective noise temperature at the reference point for each corresponding input temperature $T_{in,A}^P$. The quantities α_L and α_S are the loss coefficients for the long and short transmission lines of the radiometer. The T_L^{phy} and T_0^{phy} are the physical temperatures of the long and short transmission lines, respectively.

After estimating the ACS T_B at various internal set temperatures, one can determine a line using two points of ACS and HS T_B values for each radiometer state. The line slope and intercept (i.e., m and b) values can be estimated using (5)–(7)

$$T_{in,A}^P = Nm + b \quad (5)$$

$$m = \frac{T_B^C - T_B^H}{\alpha_L \alpha_S} \quad (6)$$

$$b = \frac{1}{\alpha_L \alpha_S} T_B^H - \frac{(1 - \alpha_L)}{\alpha_L} T_L^{phy} - \frac{(1 - \alpha_S)}{\alpha_L \alpha_S} T_0^{phy}. \quad (7)$$

The physical temperature of each of the RF components of the radiometer is recorded in real time using temperature sensors. The radiometer's internal temperature is controlled using a solid-state Peltier cell. We also controlled the room temperature of the anechoic chamber to reduce any sudden temperature changes during the measurement to minimize any noise introduced due to the temperature change.

2) External Calibration: The external calibration technique involves using external references or targets to calibrate the radiometer's measurements through the antenna. This involves well-characterized radiometric properties of known targets and can be used as a reference to produce a voltage-to-temperature calibration line. For the external calibration, the radiometer was initially placed inside an anechoic chamber. The anechoic chamber was considered as a blackbody, and the physical temperature of the blackbody was measured to be 290 K during the calibration experiment. The radiometric measurements were taken while the H-pol and V-pol antennas were pointed toward the ceiling
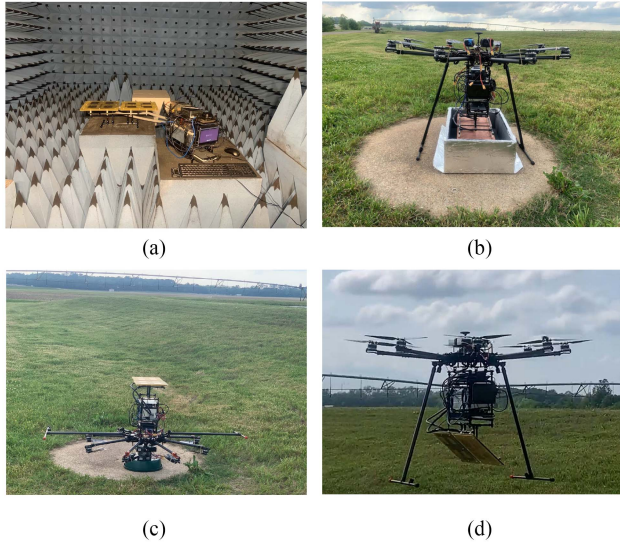
Fig. 7. External calibration of the radiometer antenna was performed using three calibration methods: anechoic chamber (blackbody) calibration, absorber (blackbody) calibration, and sky temperature measurement. (a) Calibration of the radiometer dual-polarized antenna inside the anechoic chamber (blackbody). (b) Calibration of the radiometer antenna using a small electromagnetic absorber (blackbody) box. (c) Calibration of the radiometer antenna using sky temperature measurement. (d) Radiometer antenna positioned at a 45° angle for field measurements.

Fig. 8. (a) 3-D simulated radiation pattern of the antenna. (b) Simulated and measured antenna return loss (s_{11}).

of the anechoic chamber. Fig. 7(a) shows the setup where the radiometer collects the data inside the anechoic chamber.

During the field experiment, the antenna was placed inside a small absorber (blackbody) box and took measurements for external calibration. The physical temperature of the absorber box was also recorded during the measurement. Fig. 7(b) shows the field set-up for blackbody measurements. Next, the antenna was pointed towards the sky to measure the T_B of the sky. At L-band, the T_B of the sky is considered to be 10 K. Fig. 7(c) shows the upside–down UAS setup where the antenna points toward the sky.

The antenna loss coefficient plays an important role in radiometric measurements. One can measure the antenna loss coefficients by taking the radiometric measurement of two known sources: the sky and the blackbody. The effective sky and blackbody T_B $T_{\text{in},S}^P$ at the reference point is estimated by using the internal two-point calibration using HS and ACS. The $T_{\text{in},S}^P$ is then used to measure the antenna efficiency for each antenna port using (8)

$$T_{\text{in},S}^P = T_{\text{in},A}^P \alpha_A^P \alpha_L \alpha_S + T_{\text{Ant}}^{\text{phy}} \left(1 - \alpha_A^P\right) \alpha_L \alpha_S$$
$$+ T_L^{\text{phy}} \left(1 - \alpha_L\right) \alpha_S \quad + T_0^{\text{phy}} (1 - \alpha_S) \quad (8)$$

where $T_{\text{in},A}^P$ is the effective antenna temperature, α_A^P is the loss coefficient of the antenna or antenna efficiency, and $T_{\text{Ant}}^{\text{phy}}$ is the physical temperature of the antenna.

Finally, for regular science measurements, the radiometer antenna was pointed at a 45° incidence angle toward the ground. Fig. 7(d) shows the fully configured radiometer prepared to fly and take measurements from the land surface.
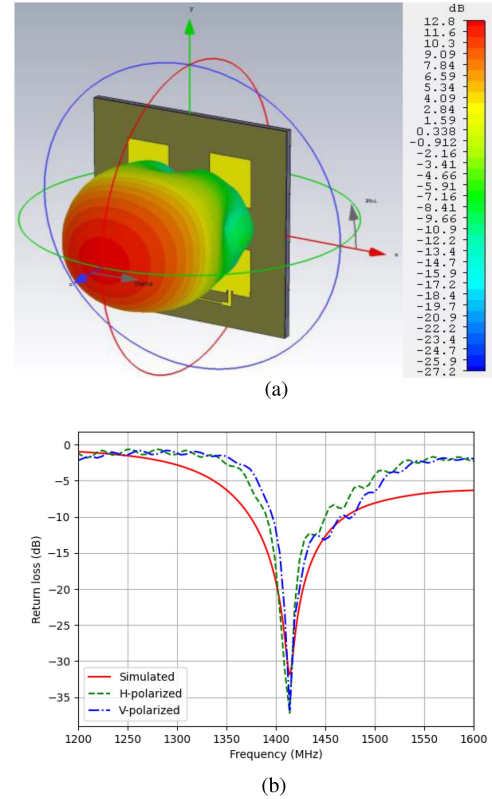
D. Custom UAS and Radiometer Footprint

A custom octacopter UAS was designed and built to carry the radiometer as payload. The temperature-controlled radiometer box was mounted underneath the UAS and flew over the land and water at the R. R. Foil Plant Science Research Center (known as the North Farm) at MSU. The UAS has flown at an altitude of 15 m with a speed of 2 m/s. The antenna half-power beam width is 37°. The antenna is observing the target at 45° angle. The major axis of the ellipse is calculated at 22.60 m, while the minor axis of the ellipse is 15.06 m.

III. RESULT

This section will describe the results of antenna characterization, several steps of data cleaning, radiometric calibration, field experiment, and finally, the results of the estimated T_B on a geospatial map.

A. Antenna Characterization

For microwave radiometry, the antenna plays a crucial role in acquiring electromagnetic radiation response from the target source. The antenna was designed in the electromagnetic simulation environment. In the design, particular attention was placed on minimizing the level of sidelobes and backlobes. Fig. 8(a) shows the 3-D simulated radiation pattern. The interelement spacing of the array and the air gap distance between the
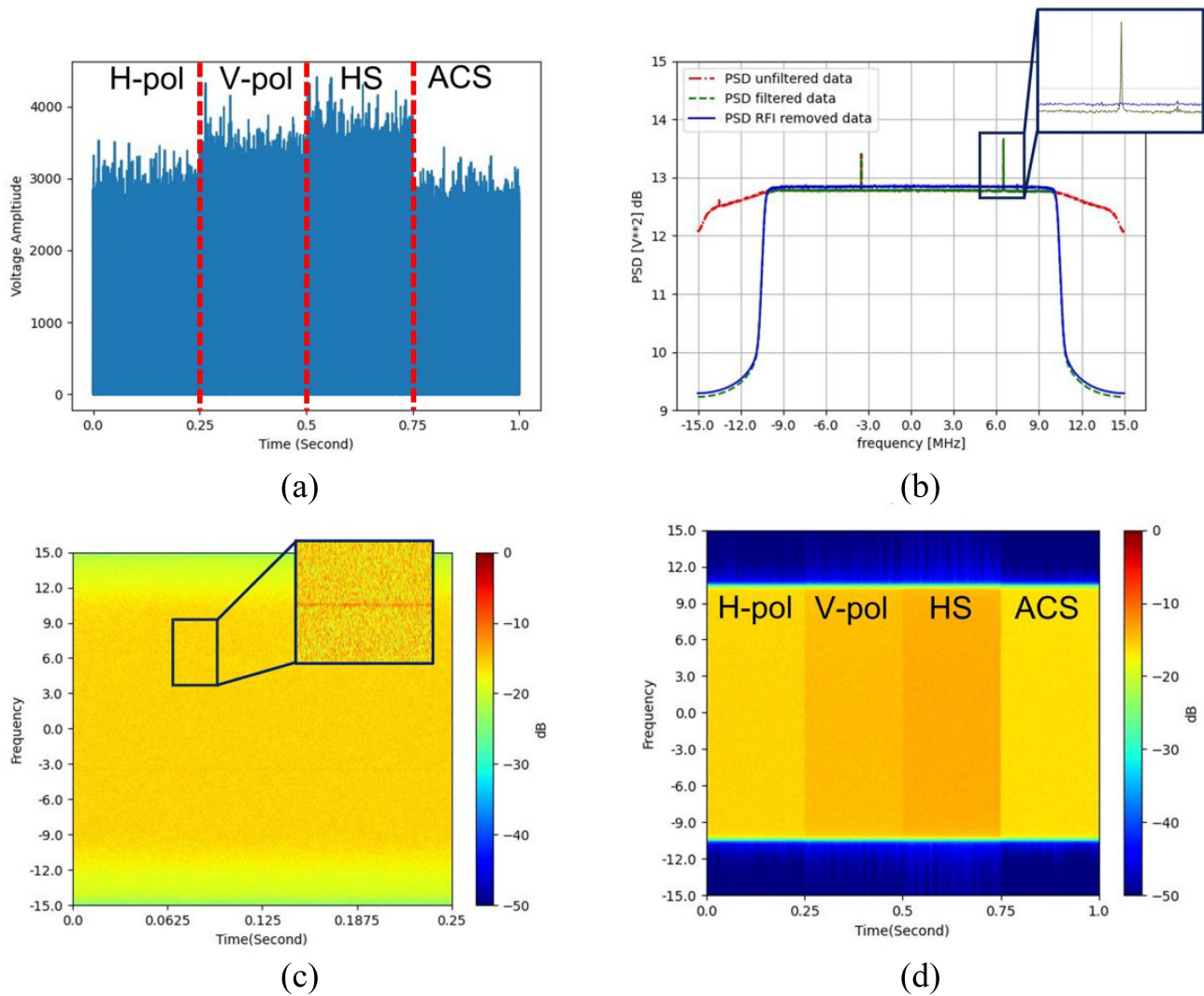
(a)

(b)

(c)

(d)

Fig. 9. Removing instrument generated RFI from raw data at each of the 250 ms segments of each cycle. (a) Raw antenna count data from four input ports of the radiometer. (b) PSD of the H-pol port signals before and after cleaning. (c) Spectrogram of the H-pol port before removing RFI. (d) Clean spectrogram of a complete cycle of 1000 ms from all four port.

front patch and ground plane were iteratively adjusted to achieve the desired gain. The same process was also used to reduce the sidelobe and the backlobe of the antenna. The antenna has a half-power beam width of $37°$. The overall gain of the array is 12.84 dB at 1413.5 MHz center frequency. The theoretical antenna return loss is calculated to be -31 dB in the simulated environment. The antenna was characterized in the anechoic chamber using a network analyzer and found -37 and -36 dB return loss at the center frequency for H-pol and V-pol antennas, respectively, as shown in Fig. 8(b). The solid red line represents the simulated return loss, whereas the green and blue dotted lines show the measured return loss for the H-pol and V-pol antennas, respectively.

B. Data Processing and Cleaning

The internal electronics of the radiometer may introduce some systematic interference into the radiometric raw (Level-0)

measurements. An example of raw data acquired in the anechoic chamber (shielded from outside) is given in Fig. 9(a), which represents the data from one complete cycle (1000 ms), consisting of four segments. Each of the segments represents 250 ms of data. In this example, the first segment of Fig. 9(a) represents the signals recorded at the H-pol port (connected to the LN noise source, no antenna is connected), and the second segment represents the data at the V-pol port (connected to the DI noise source, no antenna is connected). The third and fourth segments show the internal loads' response (i.e., HS and ACS, respectively). Internal sources might induce some unwanted bias in the measurements. For instance, the power spectral density (PSD) of the H-pol port shown in Fig. 9(b) exhibits some spikes. As we can also see in the zoomed section of Fig. 9(b), signal levels differ and can shift the overall response artificially, if those spikes are not removed. The same response can be observed in the normalized TF spectrogram in Fig. 9(c), where the bright red line is apparent in the zoomed section. After digital filtering
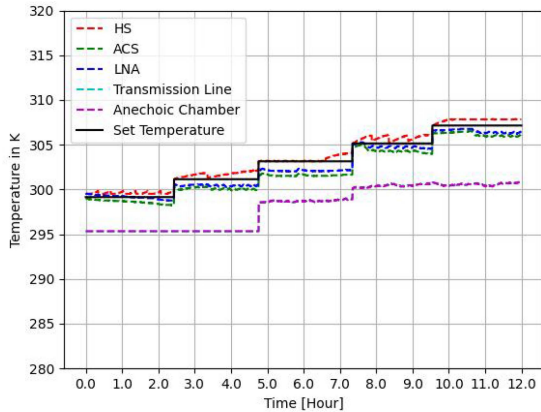
Fig. 10. Physical temperature of the internal RF components and external antenna and transmission line of the radiometer over a period of 12 h. Each staircase represents one temperature setting and shows the physical temperature stability during the experiment.
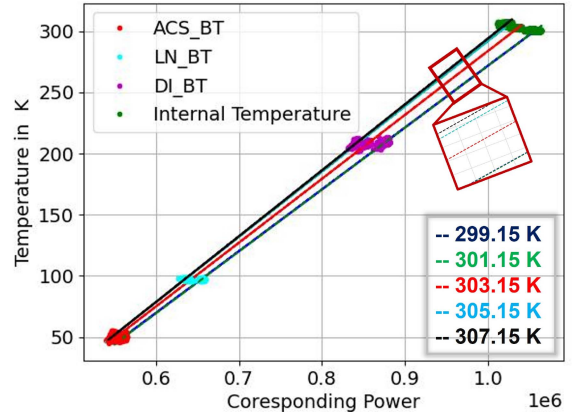

Fig. 11. Radiometer linearity line to estimate the ACS T_B for five different internal radiometer set temperatures. The zoomed red box shows five lines for five different temperature settings.

with a 10 MHz cutoff frequency and removing the instrument-generated interference, unwanted biases have been removed from the overall response for further processing, as shown in the blue color response in Fig. 9(b) zoomed section. After removing the internally generated RFI, the data from each segment of Fig. 9(a) now can be represented with a clean spectrogram in Fig. 9(d) as uncalibrated Level-1 data product.

C. Linearity Test and ACS Characterization

In this section, a linearity test was conducted, and "unknown" ACS noise temperature was characterized as a function of internal set temperatures using the interference-free measurement count as described in Section II-C. We controlled the radiometer's internal physical temperature and increased the temperature from 299.15 to 307.15 K with 2 K steps (black solid lines). The whole experiment took about 12 h, as shown in Fig. 10 where each radiometer internal temperature was set to a fixed value for about 2 h. During this time, the chamber room temperature (purple dashed lines) was also increased due to the long duration of the experiment, and as a result of the change in outdoor temperature. Even though there are some fluctuations internally, the temperature of the LNA (dark blue dashed lines) remained stable within 0.2 K for each set temperature.

We used three known sources, LN, DI, and internal temperature, or HS, to estimate the T_B of ACS. Fig. 11 shows the "linearity curve" for each of the five internal temperature settings using the responses of these four noise sources. For each radiometer internal temperature setting, we got one line consisting of four clusters of points. For instance, as we set the radiometer internal temperature 299.15 K, the estimated T_B of ACS at the switch is shown by the red dots at the left bottom corner of Fig. 11, the cyan dots represent the temperature response of the LN, the violet dots represent the temperature for DI, and finally, the green dots are the temperature of HS. From each of these lines, we estimated the T_B of the ACS for each internal temperature setting.
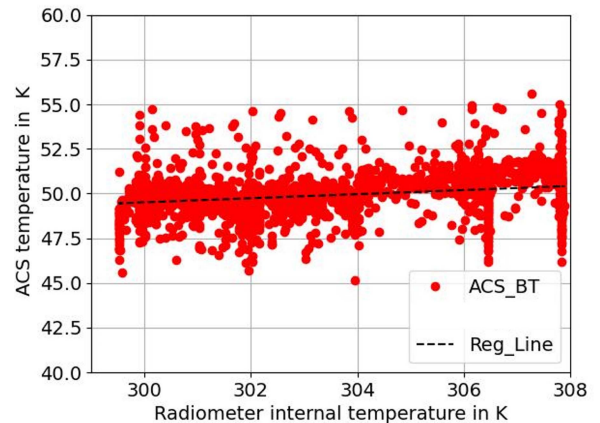
Fig. 12. Estimated ACS T_B for different radiometer internal temperature. Where the x-axis represents the change in the radiometer's internal temperature, and the y-axis shows the corresponding ACS response. Each of the red dots is the estimated temperature of ACS, and the black dotted line is the linear regression fit.

Fig. 12 shows the change of ACS T_B as we changed the internal temperature of the radiometer. The y-axis represents the ACS T_B, and the x-axis represents the change in the internal temperature of the radiometer. The red dots are the T_B response for each of the internal temperature settings, while the black dotted line is the estimated regression line. It is important to observe that the ACS noise temperature remains stable (average 49.89 K) with some fluctuations (about a standard deviation of $\pm$ 1.17 K). Since this temperature is much lower than the HS (ambient internal temperature) and is mostly independent of the internal set temperature, its impact on the internal calibration will be minimal as the measured natural T_B over land will be mostly higher than 200 K for most practical situations.

D. Radiometer Stability

After determining the internal ACS noise temperature, we tested the stability of calibrated T_B against "known" external sources (i.e., the anechoic chamber walls as the blackbody and

(a)

(b)

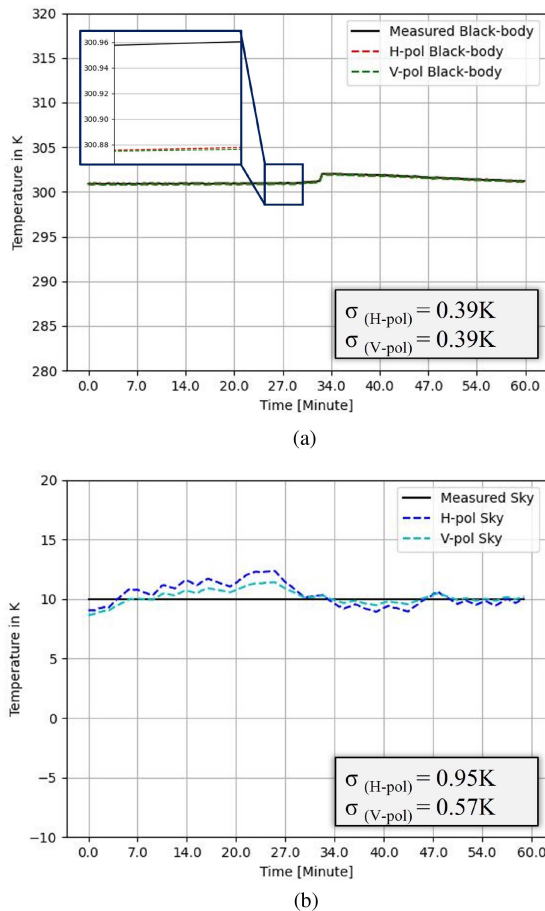Fig. 13. Measured and estimated Sky and blackbody temperature with H-pol and V-pol antennas. (a) Radiometric T_B response of a blackbody. (b) Measured and estimated sky T_B temperature response using both H-pol and V-pol antennas.
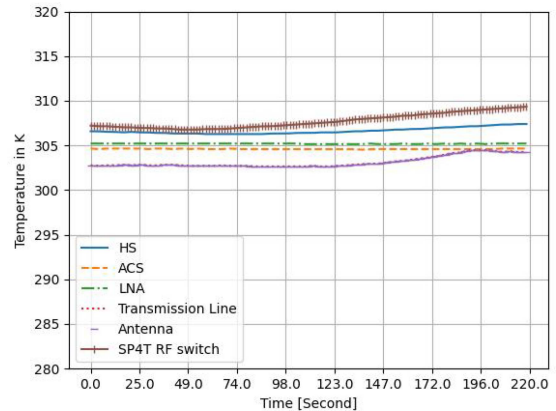

Fig. 14. Physical temperature of the internal and external RF components of the radiometer during experiment flight. Each of the lines represents the physical temperature of the RF components of the radiometer. x-axis represents the flight time in s and y-axis represents the temperature in K.

the sky). We measured the T_B of the blackbody continuously for about one hour and measured the physical temperature of the anechoic with a thermometer. We set the radiometer's internal temperature as 305.15 K during the experiment. As displayed in Fig. 13(a), the solid black line represents the measured blackbody physical temperature, and dotted lines show the estimated T_B of the blackbody with H-pol and V-pol antennas, respectively. For both polarizations, the standard deviation of the estimated T_B was calculated as 0.39 K. For instance, NASA Goddard's scanning L-band active passive (SLAP) radiometer is stable for blackbody measurement within the range of $\pm$ (1–2 K) [44]. Next, we pointed the antenna to the sky in an unobstructed environment for about 1 h, as shown in Fig. 7(c). The estimated T_B of the sky is given in Fig. 13(b). We assumed the sky T_B of 10 K as the ground truth. The dotted blue line shows the estimated T_B of the sky with the H-pol antenna, while the dotted cyan line represents the V-pol response of the sky T_B. The solid black line is 10 K as the ground truth sky T_B. We calculated the standard deviation as 0.95 and 0.57 K for H-pol and V-pol, respectively. In comparison, the uncertainty in cold sky (CS) measurement of SMAP is reported 0.11 K for H-pol and 0.09 K for V-pol [45]. These higher standard deviations for the cold sky

are expected since it is well outside of expected land observation T_B, where the radiometer is designed and calibrated.

E. Overall System Performance

In the radiometric measurements, the front-end NF is driven by the RF components (e.g., insertion losses associated with the RF components) up to the first LNA. For the present radiometer, the system noise temperature T_{sys} is calculated as 537.1 K, and the corresponding total NF as 4.4 dB using Y-technique with two "known" LN and DI sources (as described in Section II-C). The theoretical noise equivalent delta temperature (NE Δ T) using T_{sys}, bandwidth B (i.e., 27 MHz), and integration time τ (i.e., 250 ms) is calculated as 0.21 K. For example, NE Δ T for various L-band radiometers are as follows: observations of NE Δ T for SMAP over ocean and land areas reveal a value of 0.8 and 1.1 K, respectively [46]. For the SLAP instrument, NE Δ T is reported as 0.94 K for a scene temperature of 300 K [44]. The CAROLS reports an NE Δ T of 0.1 K [19], while [8] report a value of 0.14 K for an integration time of 1 ms.

F. First Flight

The first flight experiment was carried out at MSU's North Farm on 06 May, 2023. The experiment site consists of a large water body and a crop field. The UAS flight path was designed so that the radiometer footprint traverses both land and water regions on the ground. The UAS ground speed was set at a constant 2 m/s speed, and the total flight time was about 220 s.

The physical temperatures of the radiometer inside and outside were recorded during its normal operation. As seen in Fig. 14, the radiometer's internal RF components are approximately maintaining the set temperature (305.15 K). However, the antenna and the transmission line temperatures increased at the around 147th s of the UAS flight due to sunlight exposure. We used the real-time physical temperature of the radiometer's internal and external components during the T_B estimation.
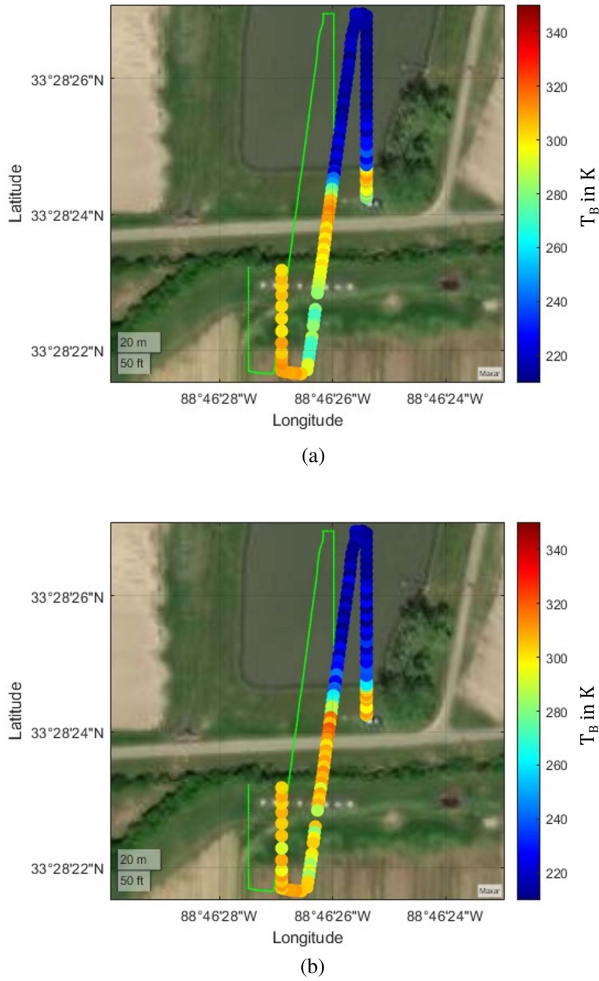
(a)

(b)

Fig. 15.   Geospatial variation of the estimated T_B. (a) T_B response with H-pol antenna. (b) T_B response with V-pol antenna. The deep green area on the top is a large water body. The light-green line is the radiometer flight path, and the colored line is the T_B response of the antenna footprint on the surface. The deep-blue colored line on the water body shows a low T_B response while the rest of the line shows varying T_B response over the field area. The Color bar on the right represents the T_B in K.

The radiometer UAS flew over the land and water combination path on the ground. In Fig. 15, the estimated T_B at both polarization's from such flight are overlaid on background imagery. The thin green line shows the UAS flight path, while the thick colored line represents the T_B measurements with a color bar. The top portion of the line shows a deep blue color, indicating the T_B response from the water body, while the varying color response represents the T_B changes on the different parts of the land cover. During the transition from water to land, the antenna footprint covers a fraction of the water region, while the rest of the path and footprint cover the land region. These mixed scenes are apparent with a light blue color at the water–land boundary. Furthermore, the starting point of the antenna footprint line shows red color as the temperature response is coming from a large metal trailer that we used as our field office during the experiment. TF analysis of the raw I&Q data revealed instances of high-power RFI. Internal instrument-generated RFI was removed from the raw I&Q

samples using the method described in Section III-B (see also Fig. 9). During the outdoor flight experiment, we attributed RFI contamination to external sources. A threshold-based algorithm was then employed to effectively remove the RFI-contaminated data points. Consequently, blank regions emerged in the spatial domain of the T_B map in Fig. 15(a) and 15(b) as a result of this RFI cleaning process. Both H-pol and V-pol antennas were able to distinguish the land and water boundary unambiguously. The T_B from both polarization's show similarities with slightly higher at V-pol, but the difference was lower than expected for an oblique incidence observation. This indicates that there is a polarization leak between the channels.

IV. DISCUSSION

This section will discuss the antenna design tradeoffs, power consumption, gross weight of the radiometer, radiometer package deployment on the UAS, and onboard data processing.

A. Antenna Design Tradeoffs

In this study, we designed and fabricated a dual polarized (H-pol and V-pol) microwave antenna for the radiometer operating in the protected L-band (1400–1427 MHz). An antenna plays a crucial role in the radiometer's operation. As we deployed our radiometer on a small UAS platform, the antenna surface area, operating bandwidth, weight, gain, return loss, sidelobes, and backlobes level were the important parameters to consider while designing the antenna. As a single patch, a microwave antenna requires a low-surface area but is prone to have low gain, high sidelobes, and backlobes levels. To achieve higher gain and low sidelobes, we designed a 2×2 array antenna as described in Section II(4). The interelement spacing of the array was carefully calculated to conglomerate four main beams of the four array elements into a single beam with combined higher gain and lower sidelobes. However, the 2×2 array structure did not help to reduce the backlobes of the antenna, which is very important for noise-free radiometric measurement. We do not want to receive any signal from the back side of the antenna. To reduce the backlobes, we introduced an air gap between the front patch and the ground plane of the antenna. The width of the air gap was carefully calculated to reduce the backlobes while maintaining the high gain of the antenna.

The H-pol and V-pol antennas were designed with identical parameters and physically rotated one antenna at 90° to acquire H-pol and V-pol response. Moreover, the cross-talk effect is important to consider while operating a dual-polarized antenna in a compact area. In our case, we place the H-pol and V-pol antennas side by side, having a small air gap in between. This can impact the purity of the polarized signal when measured at an oblique incidence. Since we did not have the facility to measure the amount of cross-talk effect of our antenna, we did not quantify the leak, but the impact was evident in the first flight measurements as mentioned previously. Further work is needed to ensure the isolation of the coupling between antennas. We attached both the H-pol and V-pol antennas on a carbon fiber frame using nylon spacers in between the frame and then the antenna. We attached the antenna frame underneath the UAS and

connected it with the receiver system using thermally insulated coaxial transmission lines.

The relatively small antenna footprint of our radiometer, measuring 22 m ×15 m along its major and minor axes, respectively, limits direct comparisons of the acquired T_B from the land–water combined area with those measured by SMAP and SMOS satellites. These satellites boast significantly larger footprints, approximately 40 [47] and 43 km [48], respectively. Furthermore, the linear correlation between land–water T_B and physical temperature presents an additional challenge for direct comparisons with other L-band radiometers [49]. Our radiometer measurements likely occurred at different geophysical locations, times, and under varying temperature conditions compared with other studies. These factors can significantly influence T_B values. While direct comparisons of our entire radiometer measurements are limited, we can analyze specific aspects related to land–water isolation. For instance, comparisons with H-pol data from [8] are possible. In addition, we can compare H-pol and V-pol data for grassland cover with studies by [50], although temperature scales might differ. In our case, the flight experiment was conducted in a hot summer day with an average ambient temperature of 307 K (34° C), we anticipated a corresponding high T_B from the radiometric measurement. Unfortunately, comparisons of our H-pol and V-pol T_B values with other L-band radiometers for similar land–water coverage and environmental conditions are not currently feasible due to the combined limitations of footprint size and potential variations in measurement conditions.

B. Power Consumption

As we designed our radiometer for the UAS-based operation, the power consumption of the radiometer is an important parameter to consider. We have limited power onboard on the UAS as a high-power battery will introduce more weight in a weight-restricted system. In our current design, the radiometer consumes a total power of ∼52.73 W during nominal operation. We used a separate battery to operate the radiometer and the UAS. The radiometer uses a six-cell lithium polymer (LiPo) battery with a voltage of 25.2 V, while the UAS uses an eight-cell 32 V LiPo battery. The UAS flight duration mainly depends on its payload weight and battery capacity. As the payload is fixed, a higher battery capacity will endure the flight time. However, the weight associated with the higher capacity battery decreases its flight time, too. So, we needed to consider the tradeoffs between the cumulative weight and battery capacity to find an optimal battery specification.

C. Weight Consideration

The weight of the payload and the weight of the UAS both contribute to the flight operation duration of the radiometer. In this study, we concentrated on the optimum operation of the radiometer with minimum expenses rather than making it lightweight. However, we kept the radiometer weight within a considerable limit so that it could be deployed as a payload on a UAS platform. In the current design, our radiometer's gross weight, including the antenna, is 20 lbs or (∼9 kg). The UAS

total weight, including the operating flight battery, is 22 lbs or (∼9.98 kg).

D. Flight Operation

In the present configuration, the radiometer flight duration is about 4 min, which covers about 480 m with 2 m/s flight speed. The flight speed of the radiometer is also critical for its ground resolution. A higher flight speed, for instance, 5 m/s will increase the coverage area but decrease ground resolution. In contrast, a lower flight speed (1 m/s) will increase the ground resolution but decrease coverage area. In our experimental flight, we used 2 m/s flight speed and had 4 min flight time. From an operational perspective, this flight duration is not sufficient to cover agricultural farms with several hectares. In the future, more emphasis needs to be placed on reducing the payload weight to improve the flight time by around 15 min while maintaining the radiometric characteristics.

E. Payload Design

We designed a custom payload attachment frame to the UAS using carbon fiber tubes. As described in Section II(3), we used a lightweight plastic box to package the radiometer in a layered structure. We covered the box using metal tape to block any RFI signal from entering the radiometer box and contaminating the radiometric measurement. We designed the carbon fiber-based payload attachment structure to carry the radiometer box inside it. We attached the antenna underneath the payload attachment frame. We affixed the antenna at a 45° angle, taking into account the aerodynamics of the UAS platform. Positioning it sideways helps mitigate wind drag, whereas a forward-facing antenna would increase drag, potentially compromising the UAS performance. The 6-inch (15.24 cm) space between the antenna and the radiometer box helps to isolate any RFI caused by the radiometer's internal electronic instruments through the small backlobes of the antenna.

F. RF Interference's

Understanding and mitigating RFI plays a pivotal role in passive microwave remote sensing measurements. Due to its potential to compromise the accuracy of geophysical parameter responses, it is imperative to detect and eliminate RFI-contaminated measurements. Traditional radiometers face challenges when dealing with RFI-contaminated measurements, often rendering recovery of any usable signal portion difficult. In contrast, our radiometer possesses the capability to store raw I&Q samples of radiometric measurements. By performing TF (spectrogram) analysis on these raw I&Q samples, we can effectively identify RFI-contaminated segments within each measurement. Our approach enables the analysis of each 250 ms or 7.5 million samples, allowing us to recover the usable portion of the signal and estimate geophysical parameters. While some resolution may be sacrificed during this process, the entirety of the measurement block is retained. In future research, we intend to implement onboard RFI processing during raw measurement collection. This processing will systematically analyze each

spectrogram of every measurement, preserving the usable data segments.

G. Data Storage

The data storage capacity is another constraint to the reliable operation of the radiometer. High storage capacity will increase the expenses and payload weight. In contrast, a lower storage will not be able to store the data in real-time operation. In our radiometer, the digital back-end preprocesses the raw radiometric measurement in near-real time while collecting continuous raw samples on the UAS platform. In the current configuration, we are operating the radiometer for a short period of time, so the storage is able to safely save the processed data along with the raw measurement data. However, looking toward the future, as the radiometer operation extends over longer durations, the current storage capacity might prove insufficient to accommodate storage requirements for all incoming measurements. In such a scenario, our approach involves the implementation of near-real-time data processing directly on the UAS platform. This entails processing the raw radiometric measurements and preserving the measured power, while selectively discarding the raw measurement data. This strategy serves the dual purpose of preserving storage space and retaining crucial information for subsequent analysis.

H. Applications

In PA, radiometric remote sensing using UAS-based radiometers holds promise for retrieving surface SM. Monitoring of high resolution surface SM can be essential to observe the changes of geophysical parameters like agricultural drought a significant threat to food security, is strongly linked to SM variations. Satellite-based monitoring of agricultural drought has been explored for global applications using Level 2 (L2) SM data products from missions, such as SMOS. Early detection of field-scale SM changes offers valuable information and can be incorporated into high-resolution agricultural drought monitoring systems [51], [52]. High spatiotemporal resolution SM data are also crucial for detecting fire events, soil erosion, and various drought types in mountainous regions. While current satellite missions offer spatial resolutions of km scale, upscaling these sparse data products can be used to estimate high-resolution SM [53]. However, uncertainties associated with validating satellite-based SM measurements against point-scale ground measurements, coupled with the influence of vegetation and topography, make high-resolution estimations challenging [54], [55]. UAS-based radiometers present a valuable tool for estimating high spatiotemporal resolution surface SM at the field scale in such scenarios. The proposed radiometer offers a ground footprint of approximately 15 m$\times$22 m at an operating altitude of 15 m. The specific spatiotemporal resolution achieved will ultimately depend on the UAS flight altitude and speed.

V. Summary and Future Work

In this study, a compact SDR-based L-band microwave radiometer was successfully developed for estimating surface T_B from a small UAS platform, allowing for efficient data collection from aerial platforms. The onboard data processing capabilities of the radiometer proved crucial in eliminating RFI contamination, ensuring the integrity of the acquired data for subsequent post-processing. A comprehensive calibration approach ensured stable radiometer measurements. This approach included in-lab calibration of the ACS against three known temperature references: LN, DI, and HS. External calibration was also performed using sky and blackbody temperatures before and after each data collection flight. This two-step process resulted in stable T_B measurements, with uncertainties of 0.39 K for both H-pol and V-pol using the blackbody, and 0.95 and 0.57 K for H-pol and V-pol, respectively, using sky measurements. Evaluation of measurement stability was conducted using sky and blackbody measurements over a 60 min period for each. These findings underscore the reliability of the radiometer's T_B measurements over an extended period. During field experiments, the radiometer was successfully attached underneath a UAS platform and flown over a land-water combination area. The radiometric response demonstrated its capability to differentiate between land and water boundaries, effectively delineating the distinctive features of the land area, such as a small roadway between the water body and the field. This capability highlights the radiometer's potential for identifying and characterizing complex land–water interfaces and land surface features.

The developed radiometer presents a valuable tool for PA applications, providing stable surface T_B estimates. The radiometer's compact design allows for easy integration beneath UAS platforms, facilitating efficient and flexible data collection. The successful removal of RFI contamination through onboard data processing ensures the reliability of the acquired data. The objective of future endeavors is to enhance the radiometer's flight time by further miniaturizing it, thereby expanding its applicability across various PA applications. The development of such a radiometer will have a significant impact on the field of PA, making it possible to improve SM estimation at subfield scale.

References

[1] V. Palazzi, S. Bonafoni, F. Alimenti, P. Mezzanotte, and L. Roselli, "Feeding the world with microwaves: How remote and wireless sensing can help precision agriculture," *IEEE Microw. Mag.*, vol. 20, no. 12, pp. 72–86, Dec. 2019.

[2] E. G. Njoku and D. Entekhabi, "Passive microwave remote sensing of soil moisture," *J. Hydrol.*, vol. 184, no. 1–2, pp. 101–129, 1996.

[3] R. Newton and J. Rouse, "Microwave radiometer measurements of soil moisture content," *IEEE Trans. Antennas Propag.*, vol. 28, no. 5, pp. 680–686, Sep. 1980.

[4] T. Schmugge and T. Jackson, "Mapping surface soil moisture with microwave radiometers," *Meteorol. Atmospheric Phys.*, vol. 54, no. 1–4, pp. 213–223, 1994.

[5] X. Wu, N. Ye, J. Walker, J. Hills, F. Jonard, and V. Pauwels, "Multiplatform radiometer systems for surface soil moisture retrieval," in *Proc. IEEE Int. Geosci. Remote Sens. Symp.*, 2019, pp. 6994–6997.

[6] R. Acevo-Herrera et al., "Design and first results of an UAV-borne l-band radiometer for multiple monitoring purposes," *Remote Sens.*, vol. 2, no. 7, pp. 1662–1679, 2010. [Online]. Available: https://www.mdpi.com/2072-4292/2/7/1662

[7] N. Ye, J. P. Walker, Y. Gao, I. PopStefanija, and J. Hills, "Comparison between thermal-optical and L-band passive microwave soil moisture remote sensing at farm scales: Towards UAV-based near-surface soil moisture mapping," *IEEE J. Sel. Topics Appl. Earth Observ. Remote Sens.*, vol. 17, pp. 633–642, Oct. 31, 2023.

[8] D. Houtz, R. Naderpour, and M. Schwank, "Portable l-band radiometer (PoLRa): Design and characterization," *Remote Sens.*, vol. 12, no. 17, 2020, Art. no. 2780.

[9] Y. H. Kerr et al., "The SMOS mission: New tool for monitoring key elements of the global water cycle," *Proc. IEEE*, vol. 98, no. 5, pp. 666–687, May 2010.

[10] S. K. Chan et al., "Assessment of the SMAP passive soil moisture product," *IEEE Trans. Geosci. Remote Sens.*, vol. 54, no. 8, pp. 4994–5007, Aug. 2016.

[11] N. J. Rodríguez-Fernández et al., "Smos-hr: A high resolution L-band passive radiometer for earth science and applications," in *Proc. IEEE Int. Geosci. Remote Sens. Symp.*, 2019, pp. 8392–8395.

[12] R. Panciera et al., "The soil moisture active passive experiments (SMAPEx): Toward soil moisture retrieval from the SMAP mission," *IEEE Trans. Geosci. Remote Sens.*, vol. 52, no. 1, pp. 490–507, Jan. 2014.

[13] M. M. Farhad, M. Kurum, and A. C. Gurbuz, "A ubiquitous GNSS-R methodology to estimate surface reflectivity using spinning smartphone onboard a small UAS," *IEEE J. Sel. Topics Appl. Earth Observ. Remote Sens.*, vol. 16, pp. 6568–6578, 2023.

[14] A. Walker, "Airborne microwave radiometer measurements during CaneX-SM10," in *Proc. 2nd SMAP Cal/Val Workshop*, 2011, pp. 1–10.

[15] G. Macelloni, S. Paloscia, P. Pampaloni, and R. Ruisi, "Airborne multifrequency L-to Ka-band radiometric measurements over forests," *IEEE Trans. Geosci. Remote Sens.*, vol. 39, no. 11, pp. 2507–2513, Nov. 2001.

[16] G. Bonin and P. Dreuillet, "The airborne sar-system: Sethi-airborne microwave remote sensing imaging system," in *Proc. 7th Eur. Conf. Synthetic Aperture Radar*, 2008, pp. 1–4.

[17] R. Baque, R. Baqué, and P. Dreuillet, "The airborne SAR-system: RAMSES NG airborne microwave remote sensing imaging system," in *Proc. IET Int. Conf. Radar Syst.*, 2012, pp. 1–4.

[18] S. S. Søbjærg, S. S. Kristensen, J. E. Balling, and N. Skou, "The airborne emirad l-band radiometer system," in *Proc. IEEE Int. Geosci. Remote Sens. Symp.*, 2013, pp. 1900–1903.

[19] M. Zribi et al., "Carols: A new airborne L-band radiometer for ocean surface and land observations," *Sensors*, vol. 11, no. 1, pp. 719–742, 2011.

[20] K. Rautiainen, J. Kainulainen, T. Auer, J. Pihlflyckt, J. Kettunen, and M. T. Hallikainen, "Helsinki university of technology L-band airborne synthetic aperture radiometer," *IEEE Trans. Geosci. Remote Sens.*, vol. 46, no. 3, pp. 717–726, Mar. 2008.

[21] T. Zhao et al., "Soil moisture retrievals using L-band radiometry from variable angular ground-based and airborne observations," *Remote Sens. Environ.*, vol. 248, 2020, Art. no. 111958.

[22] C. A. Laymon, W. L. Crosson, T. J. Jackson, A. Manu, and T. D. Tsegaye, "Ground-based passive microwave remote sensing observations of soil moisture at S-band and L-band with insight into measurement accuracy," *IEEE Trans. Geosci. remote Sens.*, vol. 39, no. 9, pp. 1844–1858, Sep. 2001.

[23] M. Kurum, R. H. Lang, P. E. O'Neill, A. T. Joseph, T. J. Jackson, and M. H. Cosh, "L-band radar estimation of forest attenuation for active/passive soil moisture inversion," *IEEE Trans. Geosci. Remote Sens.*, vol. 47, no. 9, pp. 3026–3040, Sep. 2009.

[24] M. Kurum, P. E. O'Neill, R. H. Lang, M. H. Cosh, A. T. Joseph, and T. J. Jackson, "Impact of conifer forest litter on microwave emission at L-band," *IEEE Trans. Geosci. remote Sens.*, vol. 50, no. 4, pp. 1071–1084, Apr. 2012.

[25] P. O'Neill et al., "L-band active/passive time series measurements over a growing season using the comrad ground-based SMAP simulator," in *Proc. IEEE Int. Geosci. Remote Sens. Symp.*, 2013, pp. 37–40.

[26] D. Houtz, R. Naderpour, and M. Schwank, "A cost-effective portable L-band radiometer for drone and ground-based applications," in *Proc. IEEE Int. Geosci. Remote Sens. Symp.*, 2020, pp. 6531–6534.

[27] T. K. Ho et al., "Lightweight and compact radiometers for soil moisture measurement: A review," *IEEE Geosci. Remote Sens. Mag.*, vol. 10, no. 1, pp. 231–250, Mar. 2022.

[28] A. G. Gudkov, S. V. Agasieva, I. A. Sidorov, N. F. Khokhlov, A. S. Chernikov, and Y. Vagapov, "A portable microwave radiometer for proximal measurement of soil permittivity," *Comput. Electron. Agriculture*, vol. 198, 2022, Art. no. 107076.

[29] M. M. Farhad, S. Biswas, M. A. S. Rafi, M. Kurum, and A. C. Gurbuz, "Design and implementation of a software defined radio-based radiometer operating from a small unmanned aircraft systems," in *Proc. IEEE USNC-URSI Radio Sci. Meeting (Joint With AP-S Symp.)*, 2022, pp. 17–18.

[30] M. M. Farhad, S. Biswas, A. M. Alam, A. C. Gurbuz, and M. Kurum, "SDR based agile radiometer with onboard RFI processing on a small UAS," in *Proc. IEEE Int. Geosci. Remote Sens. Symp.*, 2023, pp. 4368–4371.

[31] M. E. Nelson, "Implementation and evaluation of a software defined radio based radiometer," Ph.D. dissertation, Iowa State University, Ames, IA, USA, 2016.

[32] W. J. Blackwell, "Radiometer development for small satellite microwave atmospheric remote sensing," in *Proc. IEEE Int. Geosci. Remote Sens. Symp.*, 2017, pp. 267–270.

[33] R. F. Harrington, B. M. Grady, and C. P. Hearn, "Design and development of a microwave radiometer technology laboratory," in *Proc. Conf. Proc. Second Topical Symp. Combined Opt.- Microw. Earth Atmos. Sens.*, 1995, pp. 211–213.

[34] W. Wilson, "Earth sensing with large aperture radiometers," in *Proc. IEEE MTT-S Int. Microw. Symp. Dig.*, 1991, pp. 383–386.

[35] X. Wan, X. Li, T. Jiang, X. Zheng, L. Li, and X. Wang, "High-resolution imaging of radiation brightness temperature obtained by drone-borne microwave radiometer," *Remote Sens.*, vol. 15, no. 3, 2023, Art. no. 832.

[36] M. Peichl and S. Dill, "Detecting RFI using microwave radiometers," in *Proc. IEEE Int. Geosci. Remote Sens. Symp.*, 2012, pp. 7145–7148.

[37] A. M. Alam, M. Kurum, and A. C. Gurbuz, "Radio frequency interference detection for SMAP radiometer using convolutional neural networks," *IEEE J. Sel. Topics Appl. Earth Observ. Remote Sens.*, vol. 15, pp. 10099–10112, Nov. 18, 2022.

[38] A. M. Alam, A. C. Gurbuz, and M. Kurum, "Smap radiometer RFI prediction with deep learning using antenna counts," in *Proc. IEEE Int. Geosci. Remote Sens. Symp.*, 2022, pp. 8016–8019.

[39] S. Misra and P. de Matthaeis, "Passive remote sensing and radio frequency interference (RFI): An overview of spectrum allocations and RFI management algorithms [technical committees]," *IEEE Geosci. Remote Sens. Mag.*, vol. 2, no. 2, pp. 68–73, Jun. 2014.

[40] A. M. Alam, M. Kurum, and A. C. Gurbuz, "High-resolution radio frequency interference detection in microwave radiometry using deep learning," in *Proc. IEEE Int. Geosci. Remote Sens. Symp.*, 2023, pp. 6779–6782.

[41] W. Al-Qwider, A. M. Alam, M. Mehedi Farhad, M. Kurum, A. C. Gurbuz, and V. Marojevic, "Software radio testbed for 5G and L-band radiometer coexistence research," in *Proc. IEEE Int. Geosci. Remote Sens. Symp.*, 2023, pp. 596–599.

[42] A. M. Alam, M. Kurum, M. Ogut, and A. C. Gurbuz, "Microwave radiometer calibration using deep learning with reduced reference information and 2-D spectral features," *IEEE J. Sel. Topics Appl. Earth Observ. Remote Sens.*, vol. 17, pp. 748–765, Nov. 15, 2023.

[43] A. M. Alam, M. M. Farhad, M. Kurum, and A. Gurbuz, "An advanced testbed for passive/active coexistence research: A comprehensive framework for RFI detection, mitigation, and calibration," in *Proc. United States Nat. Committee URSI Nat. Radio Sci. Meeting (USNC-URSI NRSM)*, 2024, pp. 280–280.

[44] E. Kim, A. Wu, H. Izadkhah, and S. Abraham, "High-resolution soil moisture–a European airborne campaign using nasa goddard's scanning L-band active passive (SLAP)," *Remote Sens. Earth Syst. Sci.*, vol. 6, no. 3, pp. 309–321, 2023.

[45] J. Peng et al., "Soil moisture active/passive (SMAP) L-band microwave radiometer post-launch calibration revisit: Approach and performance," *IEEE J. Sel. Topics Appl. Earth Observ. Remote Sens.*, vol. 14, pp. 11406–11416, 2021.

[46] J. R. Piepmeier et al., "SMAP L-band microwave radiometer: Instrument design and first year on orbit," *IEEE Trans. Geosci. Remote Sens.*, vol. 55, no. 4, pp. 1954–1966, Apr. 2017.

[47] X. Cai et al., "Validation of smap soil moisture for the SMAPVEX15 field campaign using a hyper-resolution model," *Water Resour. Res.*, vol. 53, no. 4, pp. 3013–3028, 2017.

[48] Y. H. Kerr et al., "The SMOS soil moisture retrieval algorithm," *IEEE Trans. Geosci. Remote Sens.*, vol. 50, no. 5, pp. 1384–1403, May 2012.

[49] D. Long and F. Ulaby, *Microwave Radar and Radiometric Remote Sensing*. Norwood, MA, USA: Artech, 2015.

[50] D. Houtz, L. Horvath, and M. Schwank, "Vehicle mounted l-band radiometer for remote sensing of turfgrass soil moisture," in *Proc. IEEE Int. Geosci. Remote Sens. Symp.*, 2023, pp. 4824–4827.

[51] J. Martínez-Fernández, A. González-Zamora, N. Sánchez, A. Gumuzzio, and C. Herrero-Jiménez, "Satellite soil moisture for agricultural drought monitoring: Assessment of the SMOS derived soil water deficit index," *Remote Sens. Environ.*, vol. 177, pp. 277–286, 2016.

[52] P. Tarolli and W. Zhao, "Drought in agriculture: Preservation, adaptation, migration," *Innov. Geosci.*, vol. 1, no. 1, pp. 100002–1, 2023.

[53] L. Brocca, W. Zhao, and H. Lu, "High-resolution observations from space to address new applications in hydrology," *Innov.*, vol. 4, no. 3, 2023, Art. no. 100437.

[54] W. T. Crow et al., "Upscaling sparse ground-based soil moisture observations for the validation of coarse-resolution satellite soil moisture products," *Rev. Geophys.*, vol. 50, no. 2, pp. 000372–000392, 2012.

[55] A. Gruber et al., "Validation practices for satellite soil moisture retrievals: What are (the) errors?," *Remote Sens. Environ.*, vol. 244, 2020, Art. no. 111806.

Md Mehedi Farhad (Graduate Student Member, IEEE) received the B.Sc. degree in electrical and electronic engineering from the Ahsanullah University of Science and Technology, Dhaka, Bangladesh, in 2012. He is currently working toward the Ph.D. degree in electrical and computer engineering with Mississippi State University, Mississippi State, MS, USA.

He is a Research Assistant with the Information Processing and Sensing (IMPRESS) Laboratory, Mississippi State. His research interests include investigating Unmanned Aircraft Systems (UAS)-based GNSS-R techniques, Unmanned Ground Vehicle (UGV)-based GNSS-T techniques, and microwave radiometers for the remote sensing of Earth surface parameters using low-cost and smart devices.

Dr. Farhad is a Student Member of IEEE Geoscience and Remote Sensing Society. He was a recipient of Future Investigators in NASA Earth and Space Science and Technology (FINESST22) Early Carrier Research (ECR) award in 2023.

Ahmed Manavi Alam (Graduate Student Member, IEEE) received the B.S. degree in electrical and electronic engineering from the Bangladesh University of Engineering and Technology, Dhaka, Bangladesh in 2019. He is currently working toward the Ph.D. degree in electrical and computer engineering with the Mississippi State University, Starkville, MS, USA.

He was a machine learning Intern with High Performance Computing Collaboratory. He is currently Research Assistant with Information Processing and Sensing (IMPRESS) Laboratory, Mississippi State. His research interests include algorithm development of deep learning-based inverse problems and machine learning for remote sensing and physics aware deep learning.

Mr. Alam is a Student Member of IEEE Geoscience and Remote Sensing Society. He was a Finalist at the IGARSS 2022 student paper competition. He was the recipient of the National Academy of Sciences Fellowship.

Sabyasachi Biswas (Graduate Student Member, IEEE) received the B.Sc. degree in electrical and electronic engineering from the Bangladesh University of Engineering and Technology, Dhaka, Bangladesh, in 2019. He is currently working toward the Ph.D. degree in electrical and computer engineering with Mississippi State University, Mississippi State, MS, USA.

He is a Research Assistant with the Information Processing and Sensing (IMPRESS) Laboratory, Mississippi State. His research interests include radar signal processing, human activity recognition using radar, camera and lidar, and developing machine learning algorithms for activity classification using raw radar signals.

Mr. Biswas is a Member of IEEE Signal Processing Society.

Mohammad Abdus Shahid Rafi (Graduate Student Member, IEEE) received the B.S. degree in electronics and communications engineering from the Khulna University of Engineering & Technology, Khulna, Bangladesh in 2018. He is currently working toward the Ph.D. degree in electrical and computer engineering with Mississippi State University, Mississippi State, MS, USA.

He is a Graduate Research Assistant with High Performance Computing Collaboratory, Starkville, MS, and works with the Information Processing and Sensing (IMPRESS) Laboratory, Mississippi State. His research interests include remote sensing for precision agriculture, radar signal processing, Unmanned Aircraft System-based signal of opportunity reflectometry, and agricultural imaging techniques.

Mr. Rafi is a Student Member of IEEE Geoscience and Remote Sensing Society.

Ali C. Gurbuz (Senior Member, IEEE) received the B.S. degree in electrical engineering from Bilkent University, Ankara, Türkiye, in 2003, and the M.S. and Ph.D. degrees in electrical and computer engineering from the Georgia Institute of Technology, Atlanta, GA, USA, in 2005 and 2008, respectively.

In 2009, he held a Postdoctoral position with Georgia Tech, where he researched compressive sensing-based computational imaging problems. Between 2009 and 2017, he held faculty positions with TOBB University and the University of Alabama, where he pursued an active research program on the development of sparse signal representations, compressive sensing theory and applications, radar and sensor array signal processing, and machine learning. He is currently an Assistant Professor with the Department of Electrical and Computer Engineering, Mississippi State University, Mississippi State, MS, USA, where he is the Director of the Information Processing and Sensing Laboratory.

Dr. Gurbuz was the recipient of the Best Paper Award for *Signal Processing Journal* in 2013, the Turkish Academy of Sciences Best Young Scholar Award in Electrical Engineering in 2014, and NSF CAREER award in 2021. He was an Associate Editor for several journals, such as *Digital Signal Processing*, *EURASIP Journal on Advances in Signal Processing,* and *Physical Communications*.

Mehmet Kurum (Senior Member, IEEE) received the B.S. degree in electrical and electronics engineering from Bogazici University, Istanbul, Türkiye, in 2003, and the M.S. and Ph.D. degrees in electrical engineering from George Washington University, Washington, DC, USA, in 2005 and 2009, respectively.

He held Postdoctoral and Research Associate positions with the Hydrological Sciences Laboratory, NASA Goddard Space Flight Center, Greenbelt, MD, USA. From 2016 to 2022, he was an Assistant Professor with Mississippi State University (MSU), Mississippi State, MS, USA, and subsequently, he held the position of Associate Professor and the Paul B. Jacob endowed Chair until 2023. He is currently an Associate Professor in electrical and computer engineering with the University of Georgia, Athens, GA, USA, while also an Adjunct Professor with MSU. His current research focuses on recycling the radio spectrum to address the challenges of decreasing radio spectrum space for science while exploring entirely new microwave regions for land remote sensing.

Dr. Kurum is a Senior Member of IEEE Geoscience and Remote Sensing Society and a Member of U.S. National Committee for the International Union of Radio Science (USNC-URSI). He is currently the Associate Editors for IEEE Transactions on Geoscience and Remote Sensing and IEEE JOURNAL OF SELECTED TOPICS IN APPLIED EARTH OBSERVATIONS AND REMOTE SENSING since 2021. He was the recipient of the Leopold B. Felsen Award for excellence in electromagnetic in 2013 and URSI Young Scientist Award in 2014, and NSF CAREER award in 2022. He was an Early Career Representative for the International URSI Commission F (Wave Propagation and Remote Sensing) from 2014 to 2021.